



Article

Friction Stir Weldability at High Welding Speed of Two Structural High Pressure Die Casting Aluminum Alloys

Javier Vivas ^{1,*} , Ana Isabel Fernández-Calvo ² , Egoitz Aldanondo ¹ , Uxue Irastorza ¹ and Pedro Álvarez ¹

¹ LORTEK Technological Centre, Basque Research and Technology Alliance (BRTA), Arranomendia Kalea 4A, 20240 Ordizia, Spain

² AZTERLAN, Basque Research and Technology Alliance (BRTA), Aliendalde Auzunea, 6, 48200 Durango, Spain

* Correspondence: jvivas@lortek.es

Abstract: In this work, the friction stir weldability of two structural high-pressure die casting aluminum alloys designed to manufacture thin-walled automotive components is investigated and compared. AlSi10MnMg and AlMg4Fe2 alloys were friction stir welded at a high welding speed (from 500 to 2000 mm/min) for a fixed rotation speed of 1500 RPM. The investigation was performed by studying the material flow influence on defect formation and microstructure, the mechanical properties of the welds and the forces that act during the friction stir welding process. The AlSi10MnMg alloy shows a lower incidence of defects than the AlMg4Fe2 alloy at all welding speeds investigated. Both materials present a great friction stir welding performance at 500 mm/min with a high joint efficiency in terms of ultimate tensile strength: 92% in AlSi10MnMg alloy and 99% in AlMg4Fe2 alloy.



Citation: Vivas, J.; Fernández-Calvo, A.I.; Aldanondo, E.; Irastorza, U.; Álvarez, P. Friction Stir Weldability at High Welding Speed of Two Structural High Pressure Die Casting Aluminum Alloys. *J. Manuf. Mater. Process.* **2022**, *6*, 160. <https://doi.org/10.3390/jmmp6060160>

Academic Editors: Carlos Leitao, Ivan Galvão and Rui Manuel Leal

Received: 15 November 2022

Accepted: 7 December 2022

Published: 12 December 2022

Publisher's Note: MDPI stays neutral with regard to jurisdictional claims in published maps and institutional affiliations.



Copyright: © 2022 by the authors. Licensee MDPI, Basel, Switzerland. This article is an open access article distributed under the terms and conditions of the Creative Commons Attribution (CC BY) license (<https://creativecommons.org/licenses/by/4.0/>).

Keywords: friction stir welding; material flow; structural high pressure die casting; aluminum alloy; process forces; joint efficiency; weld formation

1. Introduction

Aluminum alloys are widely used in the transportation industries due to their potential to produce lightweight and strong structures [1]. However, nowadays, a transportation industry that deserves special attention from a research and development point of view for its rising interest in the applications of aluminum alloys is the automotive industry. The development of electric vehicles and their entrance in the market along with the soaring pressure of governments to reduce CO₂ emissions is forcing automotive manufacturers to invest in the research and development of aluminum alloys with the aim of achieving lightweight vehicles [2,3]. One of the research lines aligned with this goal that is gaining relevance is the development of aluminum alloys produced by special casting techniques.

The focus of the present work is high ductility die castings, known also as structural die casting or Vacuum-assisted High Pressure Die Casting (VPDC). These processes, dated from the 1990s, were focused on obtaining HPDC castings with improved mechanical properties in terms of strength and ductility by the combination of optimum alloy chemistry, melt treatment, die release agent with low gas porosity decomposition, mold and process design including the vacuum application to reduce gas entrainment [4–8]. Fundamentally, conventional HPDC consists of injecting a molten metal into a mold by high pressure. The metal becomes solidified quickly to form the final component. VPDC maintains the main advantage of HPDC casting technology that facilitates the production of thin-walled large components at great speeds and allows for obtaining an optimum mechanical performance [6–10].

Sigworth and Donahue [11] recently revised the metallurgy of aluminum alloys for structural high pressure die castings. The alloy most well-known, and in use for the longest time, is the Rheinfelden alloy Silafont[®] 36 (AlSi10MnMg alloy). It has been used

to produce numerous structural components for more than twenty years [11]. Other companies have developed similar alloys to compete with, or improve upon it. Rheinfelden has also developed similar alloys. A list of the newer alloys is showed in [11] and includes Castaduct-42 (AlMg4Fe2) alloy as an interesting alloy. AlSi10MnMg alloy provides a wide range of mechanical properties using different heat treatment temps: T4, T6 or T7. While AlMg4Fe2 alloy is only used in as-cast state because is a non-heat treatable alloy. Nevertheless, both alloys are suitable for structural applications. Comparing AlMg4Fe2 to AlSi10MnMg, AlMg4Fe2 has lower HPDC castability, higher elongation and more stable mechanical properties after long-time heating [6].

Most applications of VPDC casting aluminum alloys for the automotive industry are in the area of structural parts, such as chassis and its auxiliaries [12]. Bearing in mind that body structural applications are highly demanding in terms of strength and ductility, the joints that configure these parts must guarantee an adequate mechanical behavior. Furthermore, the process must also show a reduced cycle time and automation potential to fulfill the high manufacturer rate by the automotive industry. Thus, the joining process of these VPDC alloys must be carefully chosen and optimized. Self-piercing rivets have been driving material requirements for many applications, such as auto bodies in the past, pushing the use of high elongation materials to obtain crack-free rivets [11]. The limited weldability of VPDC castings in comparison with other high mechanical properties casting processes, such as low pressure or die gravity casting process, is mainly associated with the higher porosity tendency observed in VPDC when high temperatures are applied, as it occurs during heat treatment and/or welding processes. The porosity formation is associated to the higher gas entrainment and/or die release decomposition typical of HPDC processes.

The VPDC alloys are weldable by arc welding in a protective atmosphere or can be joined by brazing. Unfortunately, the cost for these welding technologies is high and cannot be considered as environmentally friendly. In the literature, laser beam welding (LBW) is described as a feasible process in general for VPDC alloys, but a lack of fusion is reported as the main challenge [13]. Vacuum laser beam welding improved the porosity of the weld but a declining weld bead surface quality was identified [14]. Despite many years of research, welding of VPDC castings is still a challenge because the welding defects such as porosity or slag inclusions are prone to form [14,15]. An alternative to these joining techniques that is more environmentally friendly and has demonstrated to be a promising technology to weld various kind of wrought and cast aluminum alloys is Friction Stir Welding (FSW) [16–23].

FSW facilitates obtaining high-quality and low-cost joints. It is especially remarkable its use to weld heat treatable aluminum alloys which are difficult to weld by fusion welding technologies [24–32]. Moreover, FSW has been successfully employed to weld other materials such as steel, titanium, magnesium, copper, nickel or even composite materials [33–36].

FSW was developed and patented by The Welding Institute of Cambridge (UK) in 1991. The FSW process is straightforward. The process starts with the FSW tool rotating. Then, the FSW tool plunges into the joint line of the two workpieces. The friction generated between the materials and the FSW tool heats and plasticizes the workpieces without reaching their melting point. Once the materials are plasticized, the rotating FSW tool starts moving along the joint line and produces a solid-state bond between the workpieces. As it can be sensed, along with the welding parameters, the FSW tool plays a determining role in the quality of the joint. The FSW tool controls the heat generated by friction and the material flow along the joint line and, in consequence, the defect formation and the mechanical properties of the joint [37–39]. For this reason, the friction stir weldability of an alloy cannot be evaluated only considering the incidence of defects, the microstructure and the mechanical properties of the joint, the process forces that act on the FSW tool must be considered as well [40,41]. These forces provide important information on tool life limitation [41–44]. Trimble et al. [45] showed the relevance of the FSW process forces

and their effects on machine and tool limitations. They concluded that by the analysis of the process forces, it is possible to identify a tooling design to process the workpieces more efficiently.

This work is focused on the friction stir weldability at high welding speed of two VPDC aluminum alloys, since the potential application of these alloys is the automotive industry, where the cycle time is the paramount importance and has been one of the main factors that impedes the implementation of this technology. In this work, welding speeds from 500 mm/min to 2000 mm/min are studied. The friction stir weldability is evaluated by studying the microstructure, process forces (lateral and traveling forces and torque) and mechanical properties (microhardness measurements and tensile strength) of the welds. The combined study of these factors aims to boost the understanding of the FSW process at high welding speeds by connecting the process forces, microstructure, defect formation, welding parameters and mechanical behavior.

2. Experimental Procedure

The base materials used in this work were thick sheets of 3 ± 0.2 mm. Two alloys, AlSi10MnMg and AlMg4Fe2, were manufactured by VPDC technology to achieve high mechanical properties typical of structural components. Both samples were analyzed in as-cast state. The chemical compositions of the alloys analyzed using a Spectrolab spark spectrometer are displayed in Table 1 for both alloys, \pm symbol refers to the expanded uncertainties calculated for a 95% confidence interval ($k = 2$).

Table 1. Chemical composition of AlSi10MnMg and AlMg4Fe2 alloys (wt. %).

	Chemical Composition wt. %								
	Si	Fe	Mg	Mn	Cu	Ti	Sr	Zn	Be
AlSi10MnMg	10.0 ± 0.4	0.14 ± 0.01	0.30 ± 0.01	0.68 ± 0.05	<0.040 -	0.078 ± 0.007	0.013 ± 0.001	<0.030 -	<0.030 -
AlMg4Fe2	0.050 ± 0.012	1.60 -	3.95 ± 0.15	<0.030 -	<0.040 -	<0.030 -	<0.030 -	<0.030 -	<0.030 -

To produce the FSW butt welds, sheets were cut and machined into regular welding samples, 300 mm long by 30 mm wide.

All the welds were carried out in a commercially available friction stir welding machine with a tilt angle of 1.5° . The friction stir welds were obtained by employing a fixed rotation speed of 1500 RPM and different welding speeds (500, 1000, 1500 and 2000 mm/min). The welds were performed using forge force control mode. For each welding parameter set, similar values of plunge depth were maintained based on the observed contact conditions between the shoulder and top surface of the joint.

The in-plane reaction forces on FSW conventional X axes were recorded from the signal obtained from the piston pressure transducer and Y axes forces were recorded from the load cell in the spindle carriage. Torque measurements were obtained from the transducer attached to the spindle. A frequency of 40 Hz was employed to log the process forces and torque. The used FSW tool consisted in a 3.9 mm diameter threaded cylindrical probe and a flat 12 mm diameter shoulder (Figure 1).

After welding, metallographic samples were cut from the center of the weld coupons. Standard grinding and polishing procedures were followed. Keller's reagent was used for revealing material flow and weld microstructure. The microstructure was analyzed by optical microscopy and scanning electron microscopy (SEM) as polished and after Keller's etching. Energy dispersive X-ray spectrometer (EDS) was used for studying the chemical composition of the different phases in SEM.

The transverse orientation sections of the weld coupons were used for Vickers microhardness measurements. All specimens were polished with silica before performing the microhardness profiles across the mid-thickness.

Transverse tensile properties were obtained with dog-bone type specimens. The dimensions of the tensile test specimen are shown in Figure 2. The tensile tests were carried out at room temperature at a crosshead speed of 1 mm/min. Three tensile test specimens were prepared from each welded coupon and the results are based on the average of the three specimens.

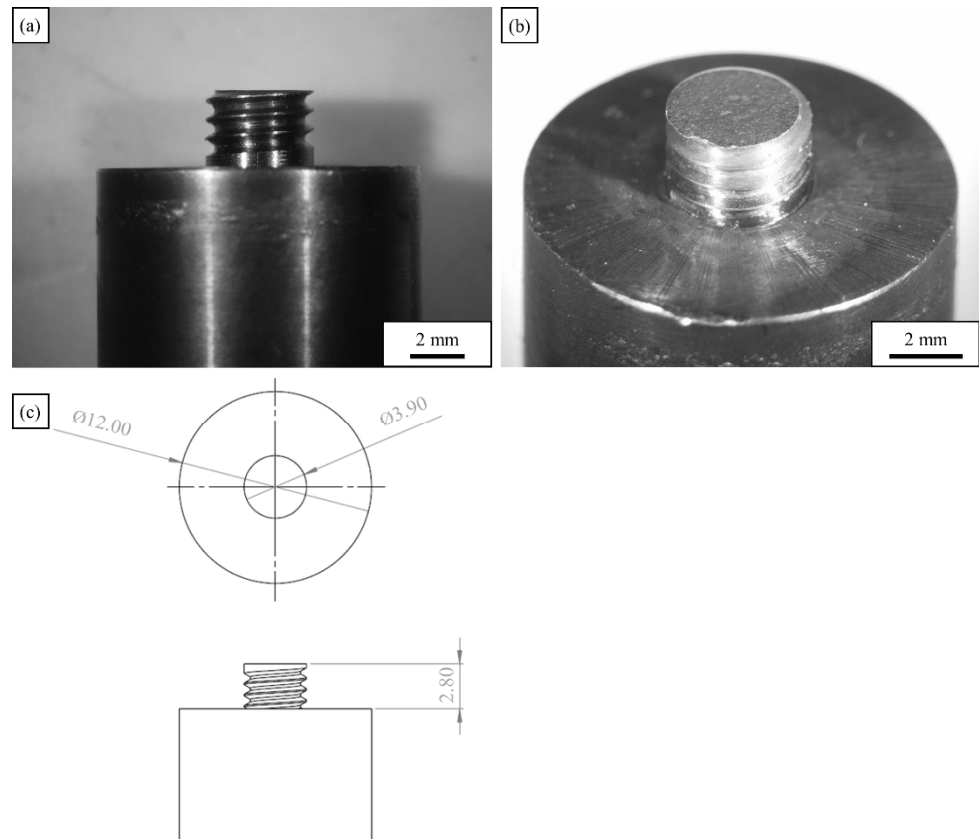


Figure 1. FSW tool. Detail of the (a) thread configuration; (b) flat shoulder; and (c) simple drawing.

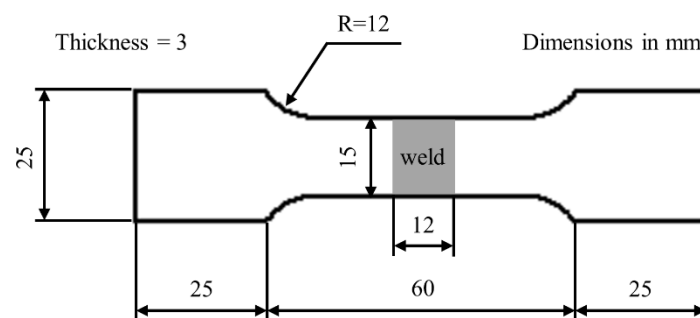


Figure 2. Tensile test specimen dimensions.

3. Results and Discussion

3.1. Microstructure: Base materials

The main microstructural characteristics of two base materials are summarized below.

3.1.1. AlSi10MnMg

The base material microstructure of AlSi10MnMg alloy shown in Figure 3 is formed by fine primary aluminum dendrites (white phases) with a fine secondary dendrite arm spacing, SDAS, around 15–20 μm due to the high solidification rate inherent to VPDC process. Hexagonal/compact and Chinese script Al-Mn-Fe-Si phases, probably $\alpha\text{-Al}_{15}(\text{Fe},\text{Mn})_3\text{Si}_2$

type phases, are observed in detail in Figure 3c; some amount of Mg and higher Si content is observed in Chinese script intermetallic particles. Very fine grey Si eutectic phases and black Mg_2Si phases (some of them indicated by arrows in Figure 3b) are also observed.

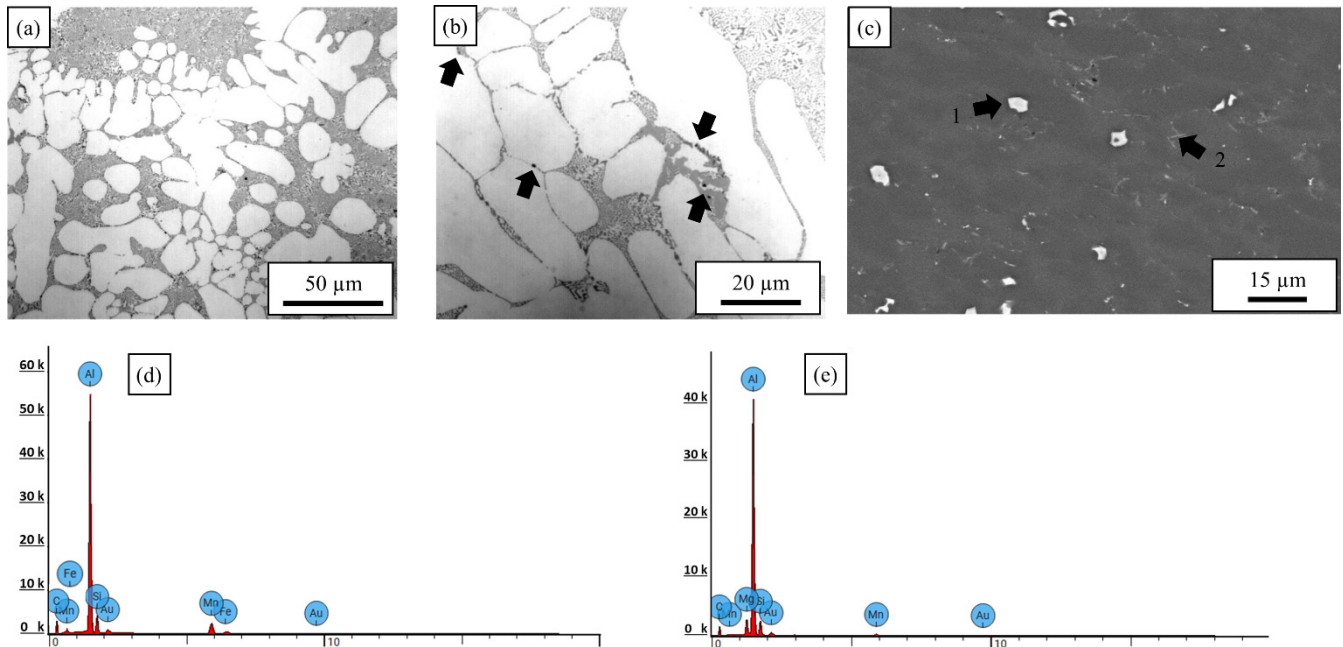


Figure 3. AlSi10MnMg base microstructure in as-cast state: (a) general microstructure view; (b) detail of Si eutectic and intermetallic particles; (c) intermetallic phases in SEM; (d) EDX of hexagonal Al-Mn-Fe-Si intermetallic particle 1 of (c); and (e) EDX of Chinese script Al-Mn-Fe-Si intermetallic particle 2 of (c).

This microstructure is the typical microstructure of an as-cast sample of primary aluminum-high silicon-manganese-magnesium alloys which is by far the most widely used type in the manufacturing of structural parts for the automotive industry by VPDC, due to their excellent castability and good mechanical properties which can be further improved by T6 heat treatment [6,8,11]. There is a balance between Fe (0.14 wt. %) and Mn content (0.68 wt. %) to avoid die soldering [46] and promote the formation of hexagonal/Chinese script type intermetallic phases instead of the harmful Fe-rich β -Al₅FeSi compounds [6,8,11, 46] which reduce the ductility due to their sharp edge morphology. Fe and Mn have a similar effect to avoid die soldering, but while Mn favors the formation of hexagonal/Chinese script type intermetallic phases, Fe favors the formation of Fe-rich β -Al₅FeSi compounds. So, Fe content must be kept low to obtain adequate ductility and avoid die soldering. Moreover, the intermetallic Al-Mn-Fe-Si phases are well below 10 microns, thus very small and evenly distributed as it is commonly observed in this type of process when Mn content is between 0.4 and 0.8 wt. % [6,8]. It should be noted that the die sticking tendency is reduced primarily by the high manganese content, but also by iron and strontium [6], favoring the manufacturing casting process.

The high modification rate of the eutectic Si is achieved by the addition of 0.013 wt. % Sr combined with the high solidification rate of VPDC process. The Sr content is within 80–350 ppm, the recommended range for AlSi10MnMg alloys [6]. Very fine (few microns length) and coral-like shape of eutectic silicon phases are the optimum characteristics to improve the mechanical properties.

3.1.2. AlMg4Fe2

The base material microstructure of AlMg4Fe2 alloy shown in Figure 4 is formed by fine primary aluminum dendrites (white phases) due to the high solidification rate of VPDC process, plate-like and Chinese script Fe-rich phases with a different content of Mg.

A small number of Al-Mg particles without any Fe content (black color in Figure 4b) are also observed. Additionally, small pores from the casting process are visible.

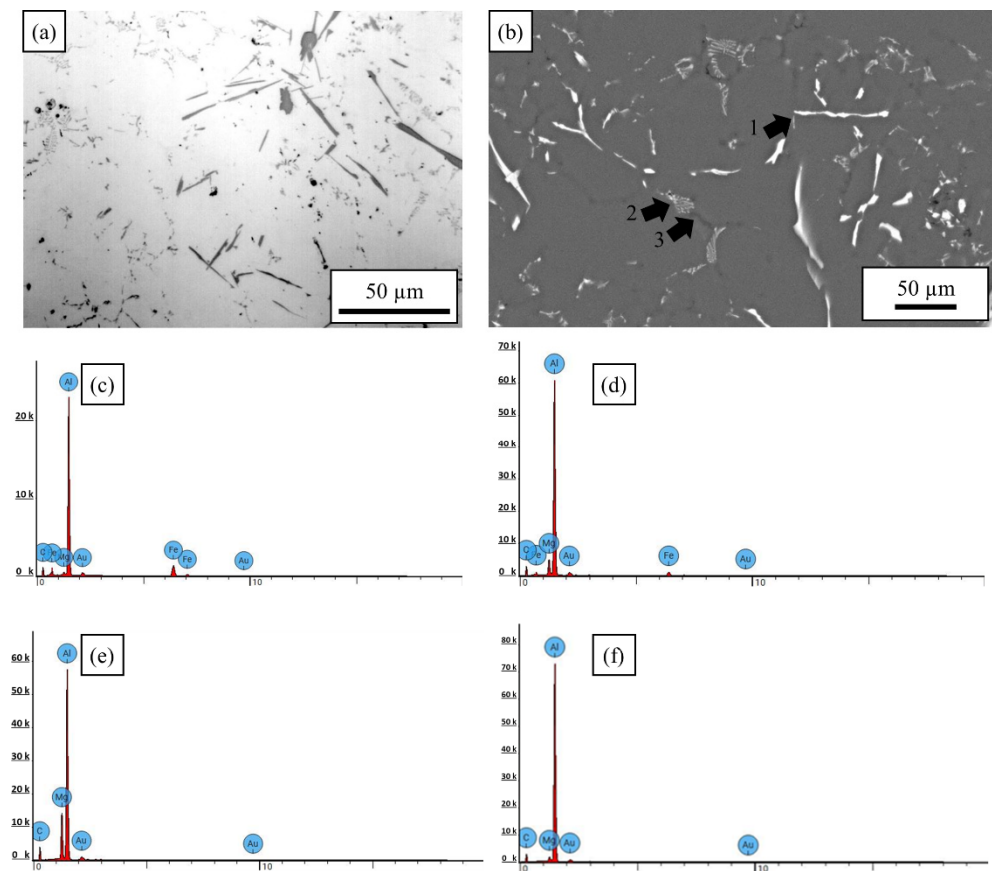


Figure 4. AlMg4Fe2 base microstructure in as-cast state: (a) general microstructure view; (b) intermetallic phases in SEM; (c) EDX of platelet-intermetallic Al-Fe-Mg particle 1 of (b) with low Mg content; and (d) EDX of Chinese script Al-Fe-Mg particle 2 of (b) with medium Mg content; (e) EDX of Al-Mg black particle 3 of (b) without any Fe content; and (f) EDX of aluminum matrix.

The high Fe content in the AlMg4Fe2 alloy (1.6 wt. %) ensures reduced die sticking tendency and improved die-casting mold life [6]. This high Mg content alloy (3.95 wt. %) is a natural-hard alloy and exhibits excellent long-term stability in the as-cast state, even at high application temperatures and it presents similar good weldability than 5xxx wrought series [6].

Aluminum solidified in fine dendrites in the VPDC process, and the Mg is dissolved in the primary solidification Al-phase [6]. $Al_{13}Fe_4$ phases are formed theoretically in this hypereutectic alloy systems. The high level of Fe led to the formation of large and plate-like Fe-containing phases (varying between 10 and 80 μm), even under the high solidification rate of VPDC process, the low Mg content in the EDX analysis (Figure 4c) is similar to the aluminum matrix value shown in Figure 4f. This platelet-shape reduces elongation. The shape and the finer size of Al-Fe-Mg Chinese scrip and Al-Mg phases are more favorable for ductility. The low Si content avoided Mg_2Si precipitation and led to an excellent ageing and dimensional stability due to the Si-free alloy composition. The low Si content below 0.2 wt. % and the absence of Mn additions avoids excessive coarsening of Fe-rich phases [6].

3.2. Microstructure: Material Flow Influence on Weld Formation

In order to study the friction stir weldability of the two VPDC aluminum alloys under investigation, the material flow influence on the defect formation and their location has been studied.

Figures 5 and 6 depict a general view of a cast aluminum alloy FSW joint (AlSi10MnMg alloy at 500 mm/min) and detail views of the different zones that composes it, respectively. In Figure 5, the retreating side is denoted by RS and the advancing side by AS. The typical microstructural zones that constitute the cast aluminum alloy FSW joints are the base material (BM), heat affected zone (HAZ), thermomechanically affected zone (TMAZ) and weld nugget (WN). The base material, the material zone unaffected by FSW, can be seen in Figure 5d and shows the characteristic base material microstructure of this casting alloy described also in Figure 3. The HAZ is the microstructural zone affected by heat. As a consequence of the heat effect, this zone usually exhibits a coarser microstructure compared to the base material, as can be appreciated in the coarser dendrite structure in Figure 5c and coarser eutectic Si in Figure 6b). The TMAZ is the zone where the material is affected by the heat and the plastic deformation. This zone is characterized by the presence of elongated, narrow and coarse phases (Figure 5a). This microstructure has been formed mainly due to dynamic recovery because the levels of temperature and strain suffered have not been sufficient to cause the dynamic recrystallization. Finally, in the WN area, aluminum dendrites and coral-like Si eutectic structures were completely broken-up by the stirring process (Figures 5b and 6c). WN presents an onion ring pattern formed by fine microstructure. An onion ring shape structure is reported to be formed by particle-rich bands, geometrical features and microstructural changes [19,21,47,48] This particular pattern has been originated by the successive shearing of the materials layers from the front to the back of the FSW tool. Its fine structure is produced by continuous dynamic recrystallization, because in contrast to the TMAZ, the heat and plastic strain have been enough to promote it [49–51].

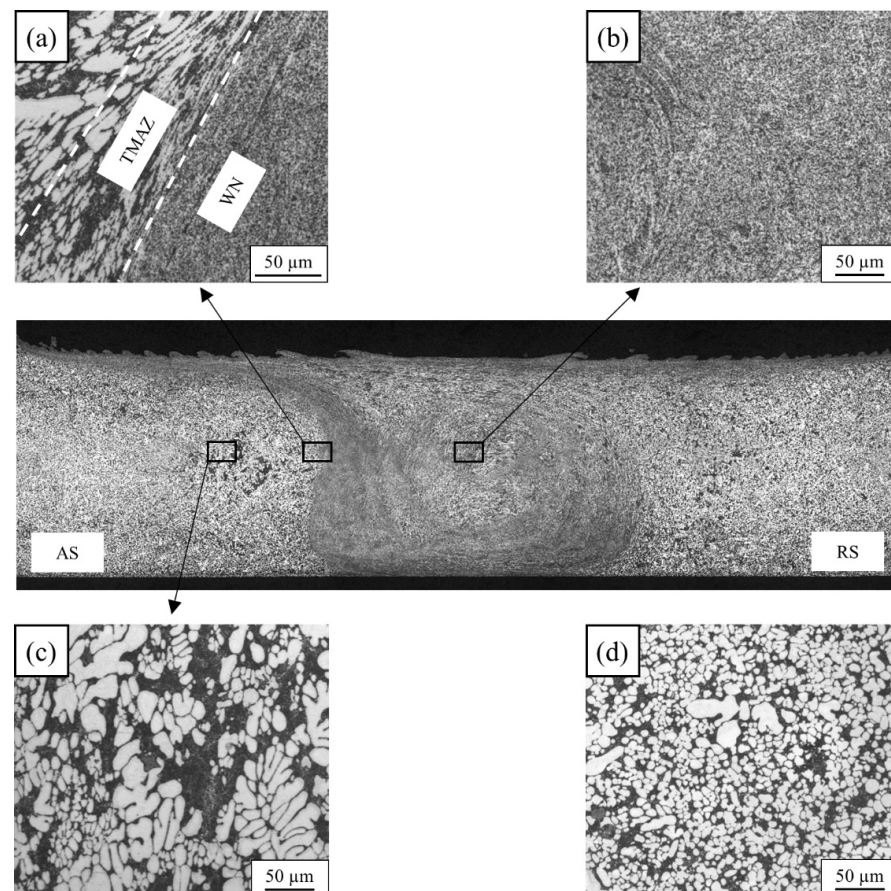


Figure 5. Cross-section and typical microstructural zones of a cast aluminum alloy FSW joint of AlSi10MnMg alloy at 500 mm/min: (a) thermomechanically affected zone (TMAZ); (b) weld nugget (WN); (c) heat affected zone (HAZ); and (d) base material.

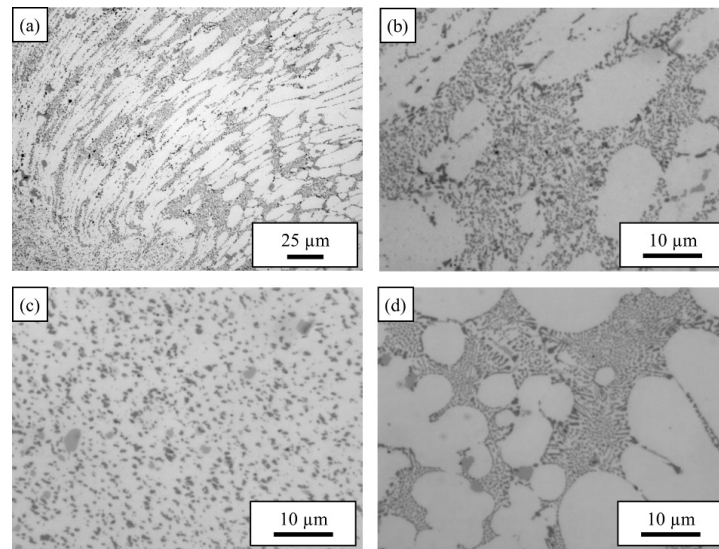


Figure 6. Detail of cross-section of AlSi10MnMg alloy at 500 mm/min: (a) TMAZ; (b) HAZ; (c) WN; and (d) base material.

Several authors reported a uniform distribution of fine and near spherical Si particles in the aluminum matrix of the stir zone for Al-high Si alloys as it is observed in the present work [18,20,23]. Finer or coarser Si eutectic particles were observed depending on the welding speed in a FSW AlSi7Mg casting alloy [18], being the Si particle size highly dependent of the tool rotation rate in Al-Si alloys [18,20]. In the present work, the size of the Si particle is very fine in comparison with a sand casting, because VPDC is one of the fastest solidifying casting processes and sand casting is one of the slowest ones. The application of heat is very effective in coarsening Si particle size as it is evident after the application of conventional T6 heat treatment. Thus, an increase in the Si particle size is expected in the HAZ, TMAZ and WN associated to the effect of heat when FSW is applied by the well-known Ostwald ripening process.

Figure 7 compares the TMAZ, WN and base material of AlMg4Fe2 at 500 mm/min. Platelet and Chinese-script Al-Fe-Mg phases are nearly spherical particles in the WN zone. Small defects are observed in the three areas. Considering their size and that they appear in the base metal and the TMAZ, these defects are attributed to the casting process itself and not to FSW process.

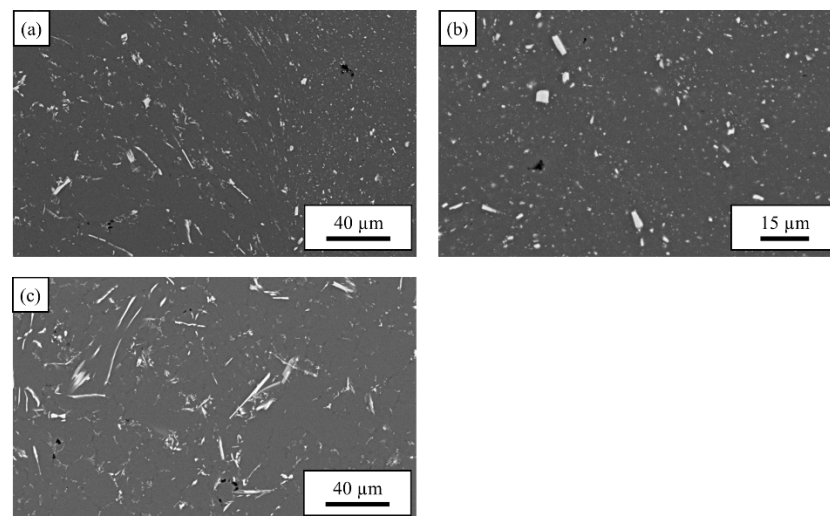


Figure 7. Detail of cross-section of AlMg4Fe2 at 500 mm/min: (a) thermomechanically affected zone (TMAZ); (b) weld nugget (WN); and (c) base material.

Figure 8 shows the transverse macro sections of the studied welds. All welds were performed at 1500 RPM and each row of images depicts the cross section for a particular welding speed.

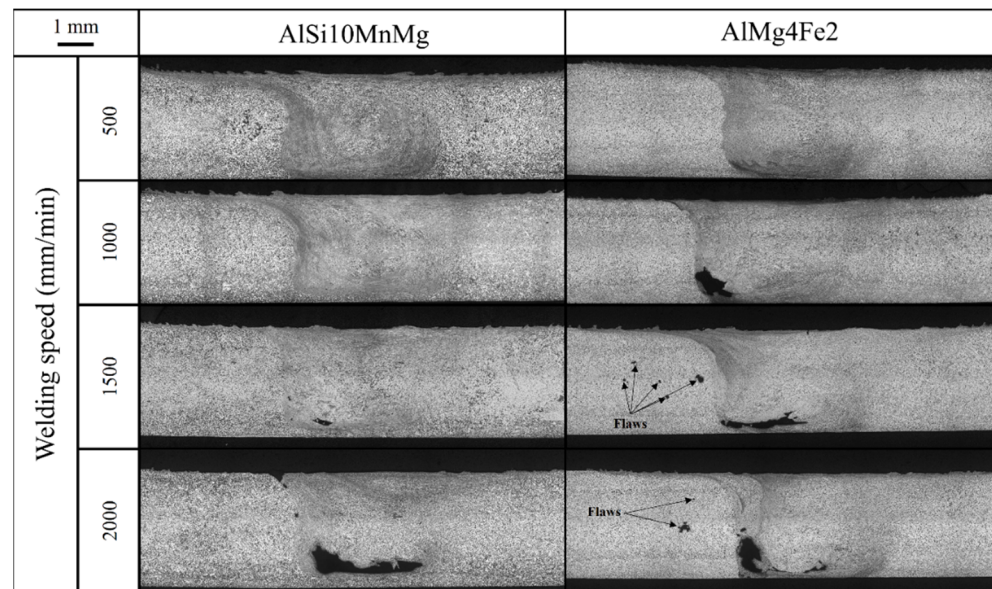


Figure 8. Macro sections of the AlSi10MnMg and AlMg4Fe2 welds. In each image the advancing side is on the left. Arrow marks indicate flaws produced during the VPDC process.

The macro sections of AlSi10MnMg show a lower incidence of defects than those of AlMg4Fe, which indicates that AlSi10MnMg has a better friction stir weldability in terms of defect formation. In any case, both alloys show defects at welding speeds higher than 500 mm/min. The defects are located in different zones depending on the welding speed. At lower welding speeds, the defects are mainly located at the bottom of the WN while at high welding speeds the defects are found at the bottom of the WN and near the border between the TMAZ and WN at the advancing side. These defects are related to an unappropriated material flow and take place outside the acceptable operation window where the welding parameters are deemed either too hot or too cold. The morphology of these defects suggests that they are wormholes/lack of fill which occur under cold welding conditions [39,52].

Figure 9 shows the area of FSW defects in AlSi10MnMg and AlMg4Fe2 welds as a function of welding speed. The area of these defects was calculated from optical micrographs by using the software ImageJ. It is observed that for the same welding speed the area of FSW defects is higher for AlMg4Fe2 than for AlSi10MnMg, except for the highest welding speed when the area of defects is quite similar. This fact highlights the superior friction stir weldability of AlSi10MnMg compared to AlMg4Fe2.

As can be observed from Figure 9, the area of the FSW defects is dependent of the welding speed. Increasing the welding speed increases the area of defects. This result can be easily explained considering that these defects are caused by cold welding conditions, as it was mentioned previously. The higher the welding speed the lower is the weld energy input, and consequently, more inefficient will be the plasticized material flow to avoid the defect formation.

Figure 10 shows some details of the evolution of FSW defects in AlSi10MnMg welds as a function of welding speed. At low welding speed (Figure 10a), small cavities are found at the bottom of the WN. While at higher welding speed (Figure 10b), the defects increase their size in this zone and appear near the border between TMAZ and WN at the advancing side. So, the defects start appearing at the bottom of the WN at a relatively low welding speed and when increasing the welding speed, the defects trend to increase their size at this area and appear at the border between TMAZ and WN heading toward the surface. When the welding speed is high enough, these wormhole defects reach the surface, as can be

observed in Figure 8 at the welding speed of 2000 mm/min for AlSi10MnMg, and generate a lack of fill. This kind of defect occurs under extremely cold welding conditions.

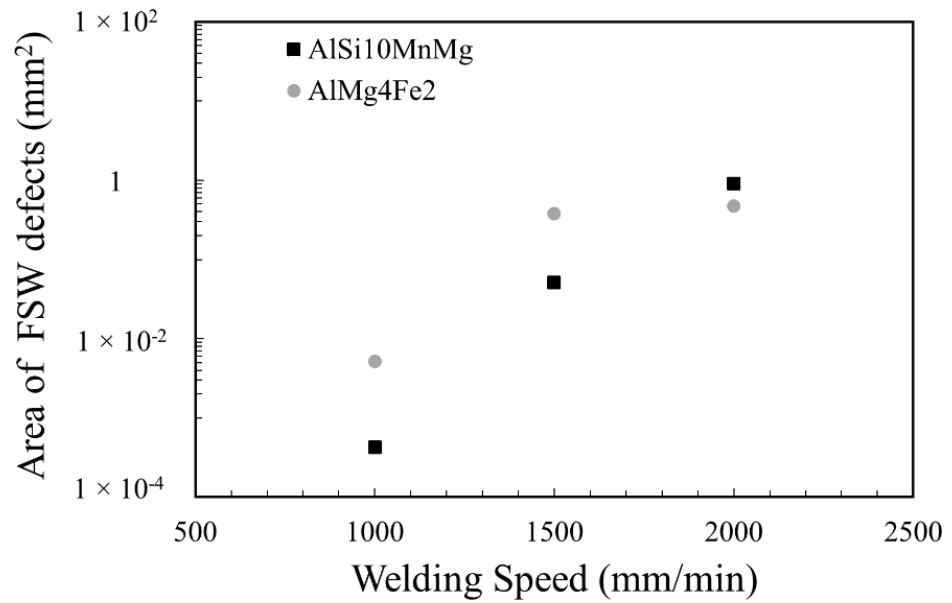


Figure 9. Area of FSW defects in AlSi10MnMg and AlMg4Fe2 welds as a function of welding speed. No value is displayed at 500 mm/min since these welds are considered free of FSW defects.

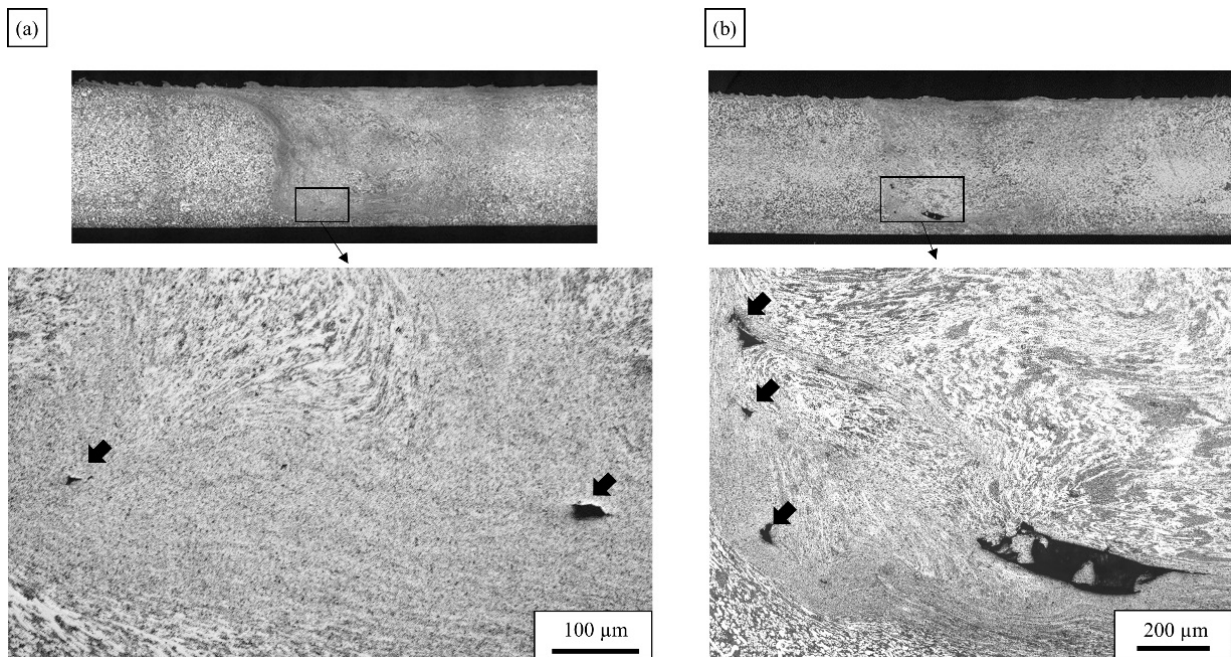


Figure 10. Evolution of defects in AlSi10MnMg welds as a function of welding speed (a) 1000 mm/min; and (b) 1500 mm/min. Arrows marks indicate the presence of small cavities in the weld.

The main reason for the presence of these defects is the insufficient amount of frictional heat. As it was explained in previous works [39,53,54], the shoulder is the most important source of frictional heat and avoids the material from flowing out of the weld. Figure 11a shows a detail of the defects located at the zone affected by the shoulder in the AlMg4Fe2 weld performed at a welding speed of 1000 mm/min. A low rotation speed combined with a high welding speed reduces considerably the friction heat generated by the shoulder and decreases the capability of the flowing material to be plasticized, and therefore, to fill the

weld cavity. This deficient material flow favors the presence of small cavities in the zone affected mainly by the material flow induced by the shoulder.

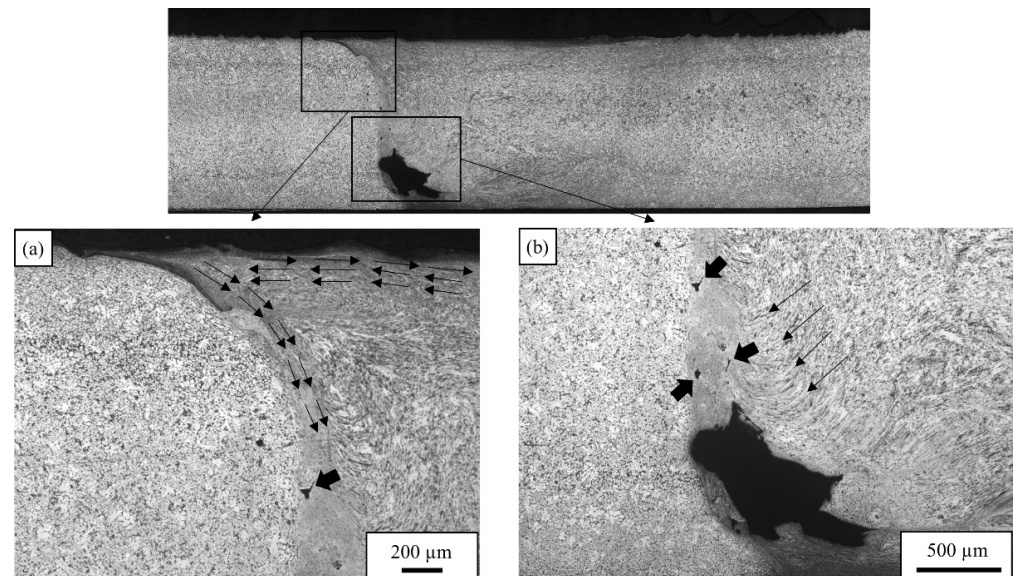


Figure 11. Detail of the defects located on the zone affected by (a) the shoulder; and (b) the probe in the AlMg4Fe2 weld performed at a welding speed of 1000 mm/min. Thin arrows indicate material flow direction and thick arrows indicate small cavities.

Concerning the defects located away from the zone affected by the shoulder, i.e., located at the bottom of the WN, the influence of the shoulder is lower and the effect of the probe starts playing a key role. Figure 11b depicts a detail of the defects located at the zone affected by the probe in the AlMg4Fe2 weld performed at a welding speed of 1000 mm/min. The probe-driven material flow depends on the temperature and the plasticization level of the workpiece materials along with the material volume transferred per second. The first ones are strongly dependent of the frictional heat generated by the shoulder while the last one is mainly controlled by the rotation speed of the probe. A low frictional heat generated by the shoulder facilitates the presence of defects at the bottom of the WN but a low rotation speed of the probe can enhance it as well. These points explain the wormholes located at the bottom of the WN in both alloys.

3.3. Process Forces and Torque during FSW

At any instant, forces are imparted on the probe by the material that flows around it. The effect of these forces moves the probe from its centerline. During transverse displacement, the probe is in contact with the material in front of it along its leading edge, which applies a compressive force on the probe surface. When the FSW tool rotates, the material is driven from the advancing side to the retreating side via the leading edge and terminates at the trailing edge of the probe. The material flows into the gap left in the probe's pathway and the shoulder introduces a vertical forging force compacting it. This material applies a compressive force to the probe from the trailing edge. Then, the resultant force that acts on the FSW tool are the forces applied by the unprocessed material from the front of the probe and the processed material from its rear. This resultant force gives useful information on the FSW tool requirements and can be visualized by using polar plots. Figure 12 shows the polar plot of average in plane-reaction resulting forces for the AlSi10MnMg and AlMg4Fe2 welds alongside the reference system employed for its set up. In this reference system, X-axis force is defined as positive in the welding direction while positive Y-force is established as the force that acts perpendicular to X direction toward

the advancing side from the retreating side. Hence, the angle and the magnitude of the in-plane reaction resulting forces are given by Equations (1) and (2), respectively:

$$\theta = \tan^{-1}\left(\frac{F_y}{F_x}\right) \tag{1}$$

$$F_r = \left(F_x^2 + F_y^2\right)^{1/2} \tag{2}$$

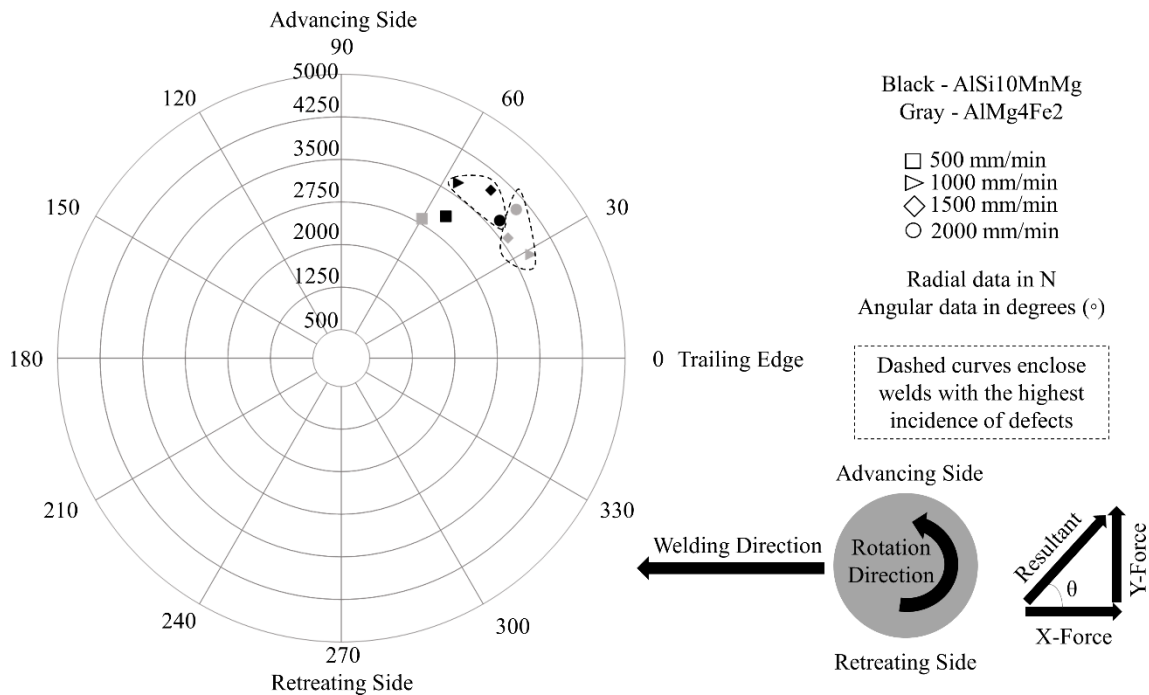


Figure 12. Polar plots of average in plane-reaction resulting forces on FSW tool for the AlSi10MnMg and AlMg4Fe2 welds.

As it can be observed in the Figure 12, all the welds are located in the first quadrant of the polar plot, the region between the advancing side and trailing edge of the probe. This result means that the material is displaced from the retreating side to the advancing side pushing the probe into the region between the advancing side and the trailing edge. For the AlSi10MnMg welds, it is observed from the polar plot in Figure 12 that increasing the welding speed increases the magnitude of in-plane reaction resulting force, except for the highest welding speed (2000 mm/min) where the magnitude of in-plane reaction resulting force has a very similar value to that obtained at a welding speed of 1000 mm/min. This trend can be explained based on the resistance induced by the plasticized material. At higher welding speeds the frictional heat is lower and the material has greater resistance to the FSW tool motion which results in a higher in-plane reaction resulting force.

Likely, the low value for the magnitude of in-plane reaction resulting force at a welding speed of 2000 mm/min may be owing to the considerable size of the defect formed at the advancing side. Many authors have studied the relationship between in-plane reaction resulting force (X-force and Y-force) and the defect formation in the weld nugget. The results of these investigations showed that in-plane reaction resulting force is influenced by the defect formation, postulating it as a promising parameter for weld quality control [55]. However, because of this force is also strongly affected by tool geometry and welding parameters [42,43,56] its relationship with the defect formation has not yet been clarified.

In the case of AlMg4Fe2 welds, no trend is observed for the magnitude of in-plane reaction resulting force. This lack of trend may have the genesis in the non-discovered

relationship between the magnitude of in-plane reaction resulting force and the defect formation. As it was commented previously, the incidence of defects was more remarkable for AlMg4Fe2 welds than for AlSi10MnMg welds (Figure 8). This higher area of defects breaks down the observed trend for AlSi10MnMg welds and demonstrates the severe impact of defect formation on the magnitude of in-plane reaction resulting force.

Table 2 summarizes the average and spread of the orientations of the in-plane reaction resulting forces for AlSi10MnMg and AlMg4Fe2 welds under all welding speeds. As observed from Table 2, the average range of orientations does not vary considerably for both alloys, however the spread of the average range of orientations is remarkably less for AlSi10MnMg than for AlMg4Fe2. From Figure 12 it can be observed that the welds with the highest incidence of defects (enclosed by dashed curves) have a lower angle of in-plane reaction resulting force compared to the welds with the lowest incidence of defects, except for the case of the AlSi10MnMg weld performed at 1000 mm/min, which has a little higher angle of in-plane reaction resulting force. However, this weld contains defects of a tiny size compared to the rest of defected welds. This tendency to reduce the angle of in-plane reaction resulting force when the incidence of defects increases suggests that the alloys with a narrower operation window, as in the case of AlMg4Fe2 compared to AlSi10MnMg, are prone to have a higher spread of the average range of orientations. This point shows that the spread of the average range of orientations can be useful to determine the friction stir weldability of an alloy in terms of incident of defects.

Table 2. Average and spread of the orientations of in-plane reaction resulting force with respect to the positive X-axis force.

Aluminum Alloy	Average Orientation (θ) With Range
AlSi10MnMg	$50^\circ \pm 7^\circ$
AlMg4Fe2	$41^\circ \pm 13^\circ$

Figure 13 exhibits the mean torque for all AlSi10MnMg and AlMg4Fe2 welds as a function of the welding speed.

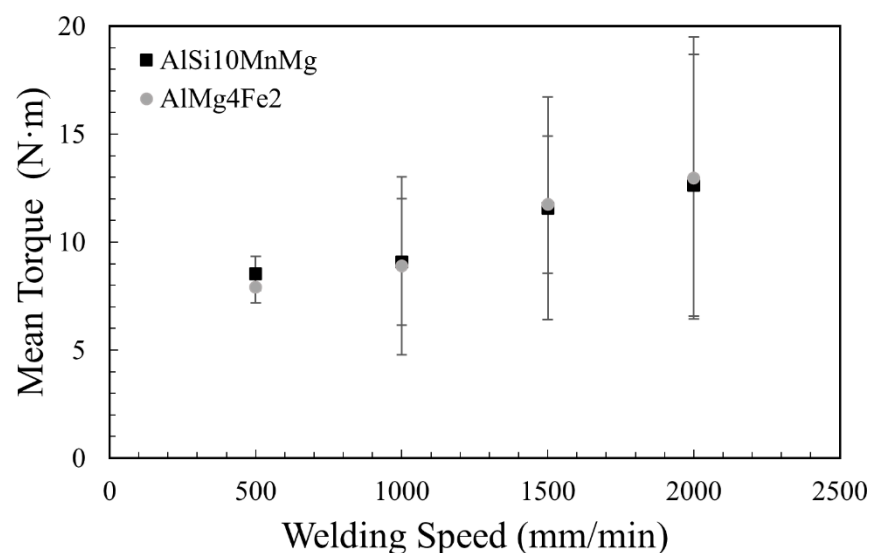


Figure 13. Mean torque as a function of welding speed for AlSi10MnMg and AlMg4Fe2 welds.

The general trend shows that increasing the welding speed increases the mean torque. As it was explained previously, increasing welding speed increases the resistance exerted by the plasticized material to FSW tool motion, which obviously increases the effort required from the FSW spindle to rotate the tool.

Comparing the values of mean torque for both alloys, all of them are very similar at the same welding speed. Thus, for the case of these alloys, torque cannot be considered a determining parameter to define what alloy possesses a better friction stir weldability.

3.4. Mechanical Properties: Microhardness Measurements and Tensile Tests

Hardness distributions transverse to the welding direction for the welds performed at 500 mm/min of AlSi10MnMg and AlMg4Fe2 are shown in Figure 14. For the AlSi10MnMg weld, the hardness profile is typical of friction stir welds in casting aluminum alloys when the peak weld temperature is close to the precipitates coarsening or solution heat treatment temperature [47,48]. The hardness distribution shape consists of a zone with lower hardness in the center (nugget), even considerably less than the hardness in the base material, surrounded by zones of higher hardness (TMAZ and HAZ). The final legs of the hardness profile are produced as the hardness values decreased with increasing distance from the weld centerline until base material hardness values are reached. Some coarse Mg_2Si particles are observed in the as-cast state of the base material in Figure 3. In addition, a high amount of Mg and Si are in unstable solid solution because this type of VPDC AlSi10MnMg casting is susceptible to T5 heat treatment [6,8]. This is associated with the high solidification rate of the VPDC process. The heat variation associated to FSW will modify the status of the strengthening Mg_2Si particles in the stirring and HAZ zone. On the other hand, Alidokht et al. [20] observed an increment in hardness after FSW of AlSi7Mg as-cast conventionally casted alloy and attributed this fact to the finer Si eutectic microstructure observed in the WN. However, a lower hardness is expected for the coarser Si structure observed in the WN zone in comparison to base material in the present work.

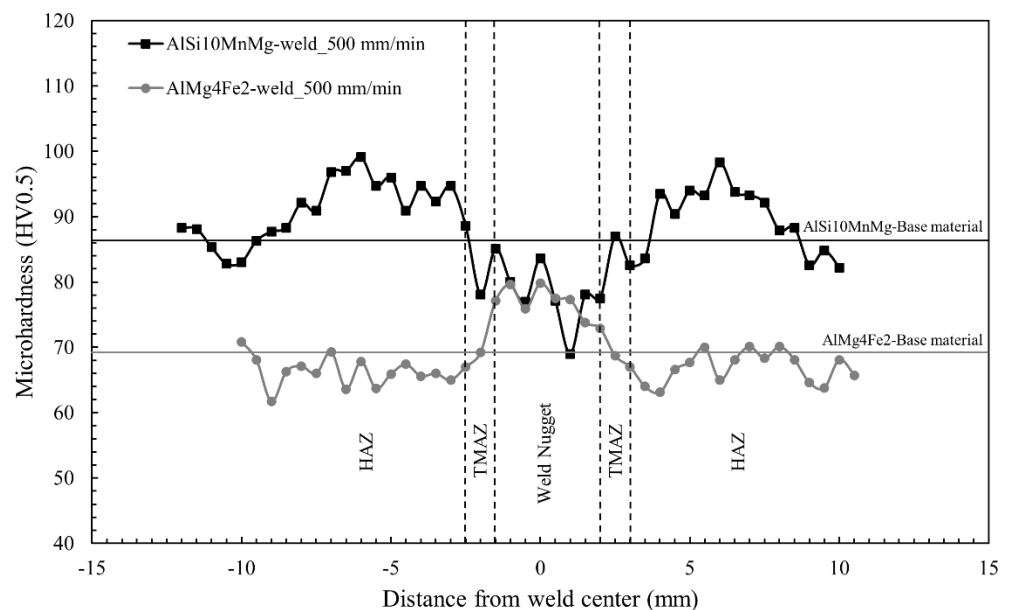


Figure 14. Microhardness profiles for the welds of AlSi10MnMg and AlMg4Fe2 performed at 500 mm/min.

Concerning the hardness profile of the AlMg4Fe2 weld, the typical shape of friction stir weld in non-hardenable aluminum alloys [57] and in Al-Mg₂Si composites [21] is observed. This shape consists of a zone of higher hardness in the center (nugget) surrounded by zones of lower hardness (TMAZ and HAZ). The highest hardness is associated to strain hardening mechanisms of AlMg alloy, similarly, to work hardening of 5XXX wrought alloys when rolling or extruding. The softening in TMAZ was also observed for FSW Al-Mg₂Si alloys [21]. The lowest hardness values (reached in the HAZ) are very close to the hardness values of the base material, which suggests that the friction stir weld does not have significant effects beyond the nugget and TMAZ. As it was aforementioned,

AlMg4Fe2 alloy has a chemical composition (high Mg and low Si content) that lead to an excellent ageing stability and thus the expected reduction in hardness is low in HAZ [6].

Table 3 summarizes the tensile test results obtained for the welds of AlSi10MnMg and AlMg4Fe2 performed at 500 mm/min. Compared to the base material, the welds exhibit slight reductions in strength and elongation. The joint efficiency in terms of ultimate tensile strength is of 92% for AlSi10MnMg and 99% for AlMg4Fe2.

Table 3. Tensile test results for the welds of AlSi10MnMg and AlMg4Fe2 performed at 500 mm/min.

Sample	Ultimate Tensile Strength (MPa)	Elongation (%)	Joint Efficiency in Terms of Ultimate Tensile Strength (%)	Fracture Location
AlSi10MnMg-Base material	290 (± 2)	6.1 (± 0.4)	-	-
AlSi10MnMg-weld_500 mm/min	268 (± 4)	4.9 (± 0.5)	92	Weld Nugget
AlMg4Fe2-Base material	265 (± 1)	16.3 (± 0.9)	-	-
AlMg4Fe2-weld_500 mm/min	263 (± 2)	14.1 (± 1.2)	99	Heat affected Zone

While the AlSi10MnMg weld was fractured by the nugget, the AlMg4Fe2 weld was fractured by the heat affected zone (Figure 15). These fracture zones are in good agreement with the hardness profiles shown in Figure 10. The lowest hardness values were obtained for the nugget in the AlSi10MnMg weld and for the heat affected zone in the AlMg4Fe2 weld, which explains that these welds were prone to fracture by these zones.

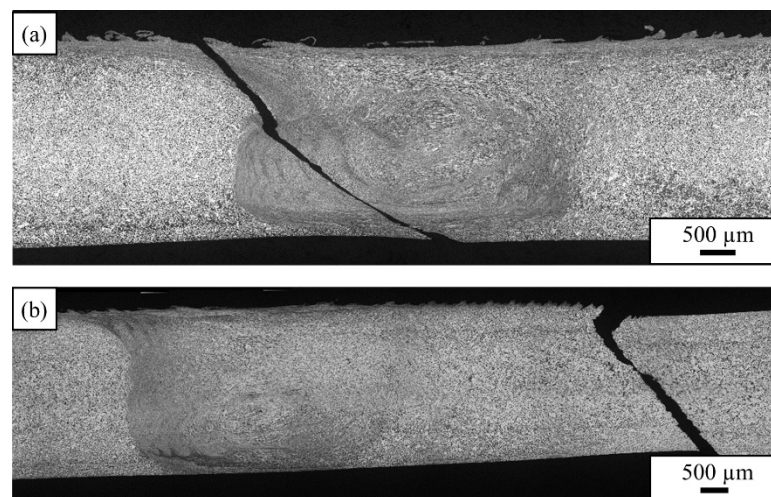


Figure 15. Cross section of fracture surface of tensile-tested specimen of (a) AlSi10MnMg; and (b) AlMg4Fe2 welds.

The higher joint efficiency for the AlMg4Fe2 implies a better friction stir weldability in terms of mechanical properties compared to AlSi10MnMg. However, AlSi10MnMg is susceptible to be easily heat-treated for increasing hardness values in the nugget, and consequently, the ultimate tensile strength and joint efficiency.

4. Conclusions

In this work, the friction stir weldability of AlSi10MnMg and AlMg4Fe2 structural high-pressure die cast aluminum alloys was investigated at a fixed rotation speed (1500 RPM) and varying the welding speed from 500 mm/min to 2000 mm/min. The main conclusions that can be drawn are:

1. As a general trend, increasing the welding speed increases the magnitude of the force imparted on the FSW tool. At higher welding speed, the frictional heat is lower and the material has greater resistance to the FSW tool motion. However, the presence of defects, such as cavities or lack of fill, diminishes the magnitude of this force due to the reduction of the plasticized material volume.

2. AlSi10MnMg VPDC alloy shows a lower incidence of FSW defects than AlMg4Fe2 VPDC alloy at all welding speeds investigated. The defects are found at the bottom of the WN and/or near the border between the TMAZ and WN at the advancing side.
3. AlSi10MnMg alloy is hardened in HAZ and softened in the middle of the FSW zone. This behavior is associated to the evolution of Mg₂Si strengthening precipitates and the coarser Si eutectic observed in the WN area. While AlMg4Fe is slightly softened in HAZ and strengthened by deformation in the middle of FSW zone.
4. At a welding speed of 500 mm/min, a high joint efficiency was obtained in both alloys in terms of ultimate tensile strength. The joint efficiency was higher for AlMg4Fe2 than for AlSi10MnMg, at 99% and 92%, respectively.

As a general conclusion, AlSi10MnMg and AlMg4Fe have great friction stir weldability at 500 mm/min achieving joint efficiency values in terms of ultimate tensile strength higher than 90%. However, the friction stir weldability decreases at higher welding speeds (1000, 1500 and 2000 mm/min) as a consequence of an insufficient material flow derived from the welding conditions being too cold.

Author Contributions: Conceptualization, J.V., E.A. and A.I.F.-C.; methodology, J.V., E.A. and A.I.F.-C.; formal analysis, J.V.; investigation, J.V., E.A., A.I.F.-C. and U.I.; data curation, J.V. and A.I.F.-C.; writing—original draft preparation, J.V.; writing—review and editing, J.V., A.I.F.-C., E.A. and P.Á.; visualization, J.V. and A.I.F.-C. All authors have read and agreed to the published version of the manuscript.

Funding: This research was partially supported by the Basque Government's Elkartek project managed by SPRI with the acronym IMAGINE and reference KK-2021/00120.

Data Availability Statement: The raw/processed data required to reproduce these findings cannot be shared at this time as the data also forms part of an ongoing study.

Conflicts of Interest: The authors declare no conflict of interest.

References

1. Sankaran, K.K.; Mishra, R.S. Chapter 4—Aluminum Alloys. Dependence of Castability and Mechanical Properties on Composition and Microstructure of Aluminum Alloys. In *Metallurgy and Design of Alloys with Hierarchical Microstructures*; Sankaran, K.K., Mishra, R.S., Eds.; Elsevier: Amsterdam, The Netherlands, 2017; pp. 57–176; ISBN 978-0-12-812068-2.
2. Giampieri, A.; Ling-Chin, J.; Ma, Z.; Smallbone, A.; Roskilly, A.P. A Review of the Current Automotive Manufacturing Practice from an Energy Perspective. *Appl. Energy* **2020**, *261*, 114074. [[CrossRef](#)]
3. Kumar, R.R.; Alok, K. Adoption of Electric Vehicle: A Literature Review and Prospects for Sustainability. *J. Clean. Prod.* **2020**, *253*, 119911. [[CrossRef](#)]
4. Hirsch, J. Recent Development in Aluminium for Automotive Applications. *Trans. Nonferrous Met. Soc. China* **2014**, *24*, 1995–2002. [[CrossRef](#)]
5. Casarotto, F.; Franke, A.J.; Franke, R. 6—High-Pressure Die-Cast (HPDC) Aluminium Alloys for Automotive Applications. In *Advanced Materials in Automotive Engineering*; Rowe, J., Ed.; Woodhead Publishing: Boston, UK, 2012; pp. 109–149; ISBN 978-1-84569-561-3.
6. RHEINFELDEN ALLOYS GmbH & Co. KG Home Page. Available online: https://rheinfelden-alloys.eu/wp-content/uploads/2018/09/rheinfelden_alloys_structural_casts_2018.pdf (accessed on 6 December 2022).
7. High Integrity Die Casting Processes | Wiley. Available online: <https://www.wiley.com/en-us/High+Integrity+Die+Casting+Processes-p-9780471201311> (accessed on 4 October 2022).
8. Niklas, A.; Baquedano, A.; Orden, S.; Noguès, E.; Da Silva, M.; Fernández-Calvo, A.I. Microstructure and Mechanical Properties of a New Secondary AlSi10MnMg(Fe) Alloy for Ductile High Pressure Die Casting Parts for the Automotive Industry. *Key Eng. Mater.* **2016**, *710*, 244–249. [[CrossRef](#)]
9. Trudonoshyn, O.; Rehm, S.; Randelzhofer, P.; Körner, C. Improvement of the High-Pressure Die Casting Alloy Al-5.7Mg-2.6Si-0.7Mn with Zn Addition. *Mater. Charact.* **2019**, *158*, 109959. [[CrossRef](#)]
10. Prach, O.; Trudonoshyn, O.; Randelzhofer, P.; Körner, C.; Durst, K. Effect of Zr, Cr and Sc on the Al–Mg–Si–Mn High-Pressure Die Casting Alloys. *Mater. Sci. Eng. A* **2019**, *759*, 603–612. [[CrossRef](#)]
11. Sigworth, G.K.; Donahue, R.J. The Metallurgy of Aluminum Alloys for Structural High-Pressure Die Castings. *Int. Metalcast.* **2021**, *15*, 1031–1046. [[CrossRef](#)]
12. Chen, Z.W.; Jahedi, M.Z. Die Erosion and Its Effect on Soldering Formation in High Pressure Die Casting of Aluminium Alloys. *Mater. Des.* **1999**, *20*, 303–309. [[CrossRef](#)]

13. Pries, H.; Rethmeier, M.; Wiesner, S.; Wohlfahrt, H. *Laser- Und Elektronenstrahlschweißen von Aluminium-Druckguss*; DVS, Ed.; Schweißen und Schneiden: Essen, Germany, 2002.
14. Teichmann, F.; Müller, S.; Dilger, K. The Influence of Ambient Pressure during Laser Beam Welding of Aluminium High Pressure Die Castings on the Occurrence of Weld Bead Porosity. In Proceedings of the Lasers in Manufacturing Conference 2017, LiM 2017, Munich, Germany, 26–29 June 2017. The German Scientific Laser Society (WLT).
15. Kah, P.; Rajan, R.; Martikainen, J.; Suoranta, R. Investigation of Weld Defects in Friction-Stir Welding and Fusion Welding of Aluminium Alloys. *Int. J. Mech. Mater. Eng.* **2015**, *10*, 26. [[CrossRef](#)]
16. Thomas, W.M.; Nicholas, E.D. Friction Stir Welding for the Transportation Industries. *Mater. Des.* **1997**, *18*, 269–273. [[CrossRef](#)]
17. Bernard, D.; Hattingh, D.G.; Goosen, W.E.; James, M.N. High Speed Friction Stir Welding of 5182-H111 Alloy: Temperature and Microstructural Insights into Deformation Mechanisms. *Met. Mater. Int.* **2020**, *27*, 2821–2836. [[CrossRef](#)]
18. Jayaraman, M.; Balasubramanian, V. Effect of Process Parameters on Tensile Strength of Friction Stir Welded Cast A356 Aluminium Alloy Joints. *Trans. Nonferrous Met. Soc. China* **2013**, *23*, 605–615. [[CrossRef](#)]
19. Tajiri, A.; Uematsu, Y.; Kakiuchi, T.; Tozaki, Y.; Suzuki, Y.; Afrinaldi, A. Effect of Friction Stir Processing Conditions on Fatigue Behavior and Texture Development in A356-T6 Cast Aluminum Alloy. *Int. J. Fatigue* **2015**, *80*, 192–202. [[CrossRef](#)]
20. Alidokht, S.A.; Abdollah-zadeh, A.; Soleymani, S.; Saeid, T.; Assadi, H. Evaluation of Microstructure and Wear Behavior of Friction Stir Processed Cast Aluminum Alloy. *Mater. Charact.* **2012**, *63*, 90–97. [[CrossRef](#)]
21. Qin, Q.; Zhao, H.; Li, J.; Zhang, Y.; Su, X. Microstructure and Mechanical Properties of Friction Stir Processed Al–Mg₂Si Alloys. *Trans. Nonferrous Met. Soc. China* **2020**, *30*, 2355–2368. [[CrossRef](#)]
22. Escobar, J.; Gwalani, B.; Olszta, M.; Silverstein, J.; Overman, N.; Bergmann, L.; dos Santos, J.F.; Staron, P.; Maawad, E.; Klusemann, B.; et al. Multimodal Analysis of Spatially Heterogeneous Microstructural Refinement and Softening Mechanisms in Three-Pass Friction Stir Processed Al-4Si Alloy. *J. Alloys Compd.* **2021**, *887*, 161351. [[CrossRef](#)]
23. Kim, Y.G.; Fujii, H.; Tsumura, T.; Komazaki, T.; Nakata, K. Effect of Welding Parameters on Microstructure in the Stir Zone of FSW Joints of Aluminum Die Casting Alloy. *Mater. Lett.* **2006**, *60*, 3830–3837. [[CrossRef](#)]
24. Kashaev, N.; Ventzke, V.; Çam, G. Prospects of Laser Beam Welding and Friction Stir Welding Processes for Aluminum Airframe Structural Applications. *J. Manuf. Process.* **2018**, *36*, 571–600. [[CrossRef](#)]
25. Wang, G.; Zhao, Y.; Hao, Y. Friction Stir Welding of High-Strength Aerospace Aluminum Alloy and Application in Rocket Tank Manufacturing. *J. Mater. Sci. Technol.* **2018**, *34*, 73–91. [[CrossRef](#)]
26. Aldanondo, E.; Arruti, E.; Alvarez, P.; Echeverria, A. Mechanical and Microstructural Properties of FSW Lap Joints. In *Friction Stir Welding and Processing VII*; Mishra, R., Mahoney, M.W., Sato, Y., Hovanski, Y., Verma, R., Eds.; Springer International Publishing: Cham, Switzerland, 2016; pp. 195–203; ISBN 978-3-319-48108-1.
27. Aldanondo, E.; Vivas, J.; Álvarez, P.; Hurtado, I. Effect of Tool Geometry and Welding Parameters on Friction Stir Welded Lap Joint Formation with AA2099-T83 and AA2060-T8E30 Aluminium Alloys. *Metals* **2020**, *10*, 872. [[CrossRef](#)]
28. Ubaid, M.; Bajaj, D.; Mukhopadhyay, A.K.; Siddiquee, A.N. Friction Stir Welding of Thick AA2519 Alloy: Defect Elimination, Mechanical and Micro-Structural Characterization. *Met. Mater. Int.* **2020**, *26*, 1841–1860. [[CrossRef](#)]
29. Wen, Q.; Li, W.; Patel, V.; Gao, Y.; Vairis, A. Investigation on the Effects of Welding Speed on Bobbin Tool Friction Stir Welding of 2219 Aluminum Alloy. *Met. Mater. Int.* **2020**, *26*, 1830–1840. [[CrossRef](#)]
30. Aldanondo, E.; Vivas, J.; Álvarez, P.; Hurtado, I.; Karanika, A. Friction Stir Welding of AA2099-T83 and AA2060-T8E30 Aluminium Alloys with New Cr-Free Surface Treatments and Sealant Application. *Metals* **2021**, *11*, 644. [[CrossRef](#)]
31. Aldanondo, E.; Zubiri, O.; Vivas, J.; Álvarez, P.; Hurtado, I. Fretting Fatigue as a Limiting Factor on the Durability of Friction Stir Welded Lap Joints Using AA2099-T83 and AA2060-T8E30 Aluminium Alloys. *J. Manuf. Mater. Process.* **2022**, *6*, 94. [[CrossRef](#)]
32. Torkamani, H.; Vivas Méndez, J.; Lecart, C.; Aldanondo Begiristain, E.; Alvarez Moro, P.; Antti, M.-L. Effect of Rotation Speed and Steel Microstructure on Joint Formation in Friction Stir Spot Welding of Al Alloy to DP Steel. *J. Manuf. Mater. Process.* **2022**, *6*, 24. [[CrossRef](#)]
33. Kubit, A.; Wydrzynski, D.; Trzepieciniski, T. Refill Friction Stir Spot Welding of 7075-T6 Aluminium Alloy Single-Lap Joints with Polymer Sealant Interlayer. *Compos. Struct.* **2018**, *201*, 389–397. [[CrossRef](#)]
34. Venu, B.; BhavyaSwathi, I.; Raju, L.S.; Santhanam, G. A Review on Friction Stir Welding of Various Metals and Its Variables. *Mater. Today Proc.* **2019**, *18*, 298–302. [[CrossRef](#)]
35. Shin, H.-S.; Jung, Y.-C.; Lee, J.-K. Influence of Tool Speeds on Dissimilar Friction Stir Spot Welding Characteristics of Bulk Metallic Glass/Mg Alloy. *Met. Mater. Int.* **2012**, *18*, 685–689. [[CrossRef](#)]
36. Gao, P.; Zhang, Y.; Mehta, K.P. Metallurgical and Mechanical Properties of Al–Cu Joint by Friction Stir Spot Welding and Modified Friction Stir Clinching. *Met. Mater. Int.* **2020**, *27*, 3085–3094. [[CrossRef](#)]
37. Nandan, R.; DebRoy, T.; Bhadeshia, H.K.D.H. Recent Advances in Friction-Stir Welding—Process, Weldment Structure and Properties. *Prog. Mater. Sci.* **2008**, *53*, 980–1023. [[CrossRef](#)]
38. Arbegast, W.J. A Flow-Partitioned Deformation Zone Model for Defect Formation during Friction Stir Welding. *Scr. Mater.* **2008**, *58*, 372–376. [[CrossRef](#)]
39. Kumar, K.; Kailas, S.V. The Role of Friction Stir Welding Tool on Material Flow and Weld Formation. *Mater. Sci. Eng. A* **2008**, *485*, 367–374. [[CrossRef](#)]
40. Balasubramanian, N.; Gattu, B.; Mishra, R.S. Process Forces during Friction Stir Welding of Aluminium Alloys. *Sci. Technol. Weld. Join.* **2009**, *14*, 141–145. [[CrossRef](#)]

41. Hattingh, D.G.; Blignault, C.; van Niekerk, T.I.; James, M.N. Characterization of the Influences of FSW Tool Geometry on Welding Forces and Weld Tensile Strength Using an Instrumented Tool. *J. Mater. Process. Technol.* **2008**, *203*, 46–57. [[CrossRef](#)]
42. Reza-E-Rabby, M.; Reynolds, A.P. Effect of Tool Pin Thread Forms on Friction Stir Weldability of Different Aluminum Alloys. *Procedia Eng.* **2014**, *90*, 637–642. [[CrossRef](#)]
43. Reza-E-Rabby, M.; Tang, W.; Reynolds, A.P. Effects of Thread Interruptions on Tool Pins in Friction Stir Welding of AA6061. *Sci. Technol. Weld. Join.* **2018**, *23*, 114–124. [[CrossRef](#)]
44. Reza-E-Rabby, M.; Reynolds, A.P. Some Effects of Tool Geometric Features on Friction Stir Weld Response Parameters. *Sci. Technol. Weld. Join.* **2018**, *23*, 575–584. [[CrossRef](#)]
45. Trimble, D.; Monaghan, J.; O'Donnell, G.E. Force Generation during Friction Stir Welding of AA2024-T3. *CIRP Ann.* **2012**, *61*, 9–12. [[CrossRef](#)]
46. Meeting, M. Metals and Materials Society. In *Light Metals 1995: Proceedings of the Technical Sessions Presented by the TMS Light Metals Committee at the 124th TMS Annual Meeting, Las Vegas, 12–16 February 1995*; Minerals, Metals & Materials Society: Pittsburgh, PA, USA, 1995.
47. Jacquin, D.; Guillemot, G. A Review of Microstructural Changes Occurring during FSW in Aluminium Alloys and Their Modelling. *J. Mater. Process. Technol.* **2021**, *288*, 116706. [[CrossRef](#)]
48. Heidarzadeh, A.; Mironov, S.; Kaibyshev, R.; Çam, G.; Simar, A.; Gerlich, A.; Khodabakhshi, F.; Mostafaei, A.; Field, D.P.; Robson, J.D.; et al. Friction Stir Welding/Processing of Metals and Alloys: A Comprehensive Review on Microstructural Evolution. *Prog. Mater. Sci.* **2021**, *117*, 100752. [[CrossRef](#)]
49. Liu, H.J.; Fujii, H.; Nogi, K. Microstructure and Mechanical Properties of Friction Stir Welded Joints of AC4A Cast Aluminium Alloy. *Mater. Sci. Technol.* **2004**, *20*, 399–402. [[CrossRef](#)]
50. Padhy, G.K.; Wu, C.S.; Gao, S. Friction Stir Based Welding and Processing Technologies—Processes, Parameters, Microstructures and Applications: A Review. *J. Mater. Sci. Technol.* **2018**, *34*, 1–38. [[CrossRef](#)]
51. Da Silva, A.A.M.; Aldanondo, E.; Alvarez, P.; Echeverria, A.; Eiersebner, M. Mechanical and Microstructural Investigation of Dissimilar Resistance and Friction Stir Spot Welds in AA5754-H22 and AA6082-T6 Al Alloys and 22MnB5 Hot-Stamped Boron Steel. In *Friction Stir Welding and Processing VI*; John Wiley & Sons, Ltd.: Hoboken, NJ, USA, 2011; pp. 389–399; ISBN 978-1-118-06230-2.
52. Kim, Y.G.; Fujii, H.; Tsumura, T.; Komazaki, T.; Nakata, K. Three Defect Types in Friction Stir Welding of Aluminum Die Casting Alloy. *Mater. Sci. Eng. A* **2006**, *415*, 250–254. [[CrossRef](#)]
53. Fonda, R.; Reynolds, A.; Feng, C.R.; Knipling, K.; Rowenhorst, D. Material Flow in Friction Stir Welds. *Metall. Mater. Trans. A* **2013**, *44*, 337–344. [[CrossRef](#)]
54. Guerra, M.; Schmidt, C.; McClure, J.C.; Murr, L.E.; Nunes, A.C. Flow Patterns during Friction Stir Welding. *Mater. Charact.* **2002**, *49*, 95–101. [[CrossRef](#)]
55. Boldsai Khan, E.; Corwin, E.M.; Logar, A.M.; Arbegast, W.J. The Use of Neural Network and Discrete Fourier Transform for Real-Time Evaluation of Friction Stir Welding. *Appl. Soft Comput.* **2011**, *11*, 4839–4846. [[CrossRef](#)]
56. Mishra, D.; Roy, R.B.; Dutta, S.; Pal, S.K.; Chakravarty, D. A Review on Sensor Based Monitoring and Control of Friction Stir Welding Process and a Roadmap to Industry 4.0. *J. Manuf. Process.* **2018**, *36*, 373–397. [[CrossRef](#)]
57. Hovanski, Y.; Upadhyay, P.; Carsley, J.; Luzanski, T.; Carlson, B.; Eisenmenger, M.; Soulami, A.; Marshall, D.; Landino, B.; Hartfield-Wunsch, S. High-Speed Friction-Stir Welding to Enable Aluminum Tailor-Welded Blanks. *JOM* **2015**, *67*, 1045–1053. [[CrossRef](#)]